

NuSTAR hard X-ray studies of the pulsar wind nebula 3C 58

HONGJUN AN¹

¹*Department of Astronomy and Space Science,
Chungbuk National University, Cheongju, 28644, Republic of Korea*

ABSTRACT

We report on new *NuSTAR* and archival *Chandra* observations of the pulsar wind nebula (PWN) 3C 58. Using the X-ray data, we measure energy-dependent morphologies and spatially-resolved spectra of the PWN. We find that the PWN size becomes smaller with increasing energy and that the spectrum is softer in outer regions. In the spatially integrated spectrum of the PWN, we find a hint of a spectral break at ~ 25 keV. We interpret these findings using synchrotron-radiation scenarios. We attribute the size change to the synchrotron burn-off effect. The radial profile of the spectral index has a break at $R \sim 80''$, implying a maximum electron energy of ~ 200 TeV which is larger than a previous estimate, and the 25-keV spectral break corresponds to a maximum electron energy of ~ 140 TeV for an assumed magnetic field strength of $80 \mu\text{G}$. Combining the X-ray data and a previous radio-to-IR SED, we measure a cooling break frequency to be $\sim 10^{15}$ Hz, which constrains the magnetic-field strength in 3C 58 to be $30\text{--}200 \mu\text{G}$ for an assumed age range of $800\text{--}5000$ years.

Keywords: ISM: individual (3C 58) — ISM: jets and outflows — X-rays: ISM — stars: winds, outflows

1. INTRODUCTION

Pulsar wind particles are believed to be accelerated to very high energies in the termination shock of pulsar wind nebulae (PWNe; e.g., [Kennel & Coroniti 1984](#)), and the energetic particles emit radiation across the whole electromagnetic waveband as observed in broadband spectral energy distributions (SEDs) of young PWNe. The emission is often modeled with synchrotron and inverse-Compton radiation (e.g., [Bucciantini et al. 2011](#)), where interaction of particles and magnetic fields produces synchrotron emission in the radio to X-ray band, and the particles upscatter soft photons (e.g., CMB, IR and optical backgrounds) to produce high-energy GeV to TeV photons (e.g., [Aleksić et al. 2014](#)). In this scenario, the X-ray SED is particularly important as it is a direct imprint of the particle distribution at the highest-energy range (e.g., [Kargaltsev et al. 2017](#)), and the maximum particle energy can help to understand particle acceleration in relativistic shocks of PWNe (e.g., [Sironi et al. 2015](#)). Particle distributions in PWNe were inferred from their photon spectra for

some young PWNe, but high-energy cutoffs in the photon spectra corresponding to the maximum electron energies were measured only for a few sources.

As particles flow in a PWN, the particles lose their energy to radiation and become less energetic with distance from the central pulsar. This effect can be seen in morphologies, spectral maps (e.g., [An et al. 2014a](#); [Kargaltsev et al. 2017](#)), and spatially-integrated spectra (e.g., [Nynka et al. 2014](#); [Madsen et al. 2015a](#)) in the X-ray band. A change of the morphology can tell us about evolution of magnetic field and particle density (e.g., [Reynolds 2009](#)), and spatial variation of the spectrum can be used to study particle flow in PWNe (e.g., [Tang & Chevalier 2012](#)). These studies have been conducted for X-ray bright PWNe (see [Reynolds et al. 2017](#), for a review).

The TeV-detected PWN 3C 58 powered by a 65-ms pulsar (PSR J0205+6449; [Murray et al. 2002](#)) is a young object possibly associated with SN 1181 ([Stephenson 1971](#)). The association is not very firm as speed of radio expansion ([Bietenholz et al. 2001](#)) or optical knots ([Fesen 1983](#)) suggests that the age may be larger, perhaps close to the pulsar spin-down age of 5000 yr. The distance to the PWN is estimated to be 2 kpc ([Kothes 2013](#)) or 3 kpc ([Roberts et al. 1993](#)) with H I observations. The distance and age inferred from observations

Corresponding author: Hongjun An
hjan@cbnu.ac.kr

Table 1. Summary of X-ray observations used in this work

Observatory	Obs. ID	Instruments	Exposure (ks)
<i>Chandra</i>	1848	HRC-S	33
<i>Chandra</i>	2756	HRC-S	24
<i>Chandra</i>	3832	ACIS-S	136
<i>Chandra</i>	4382	ACIS-S	167
<i>Chandra</i>	4383	ACIS-S	39
<i>NuSTAR</i>	30301011001	FPMA,B	81

may be somewhat correlated (Kothes 2013), and an independent estimation of the age can be made with X-ray SED measurements and time-evolving PWN models (e.g., Slane et al. 2008).

Because 3C 58 is an intriguing PWN with torus-jet structure, it was intensively studied in the soft (< 8 keV) X-ray band (e.g., Torii et al. 2000; Bocchino et al. 2001; Slane et al. 2004). Although its soft X-ray spectrum is well modeled with a simple power law, it is important to see if the spectrum extends to hard X-ray band above 10 keV. This can be done with *NuSTAR* (Harrison et al. 2013) and may give us new insights into particle acceleration and transport in PWNe. Although *NuSTAR* angular resolution is not sufficient to separate the pulsar from the PWN (An et al. 2014b), the low beaming fraction of PSR J0205+6449 (< 0.2 ; Livingstone et al. 2009; Kuiper et al. 2010) allows temporal separation of the two emission components, and hence hard X-ray properties of the PWN can be well studied with *NuSTAR*.

Here we report on X-ray observations of 3C 58 made with *NuSTAR* and *Chandra*. We measure energy-dependent morphology, spatial variation of the spectral index, and a spatially integrated broadband X-ray spectrum. These measurements are used to infer properties of 3C 58 with synchrotron-radiation scenarios. We present analysis results in Sections 2 and construct a broadband SED in the radio to X-ray band in Section 3. We then discuss and conclude in Section 4.

2. OBSERVATIONAL DATA AND ANALYSIS

2.1. Data reduction

We use new *NuSTAR* and archival *Chandra* data shown in Table 1. We process the data using `nustardas` integrated in HEASOFT 6.24 and `chandra_repro` of CIAO 4.10 along with the most recent calibration data files. Note that we use strict filters (`saamode=optimized` and `tentacle=yes`) for the *NuSTAR* data process to reduce background around South Atlantic Anomaly (SAA) passage.

2.2. X-ray timing analysis

X-ray and gamma-ray timing studies of the pulsar PSR J0205+6449 have been done previously (e.g.,

Livingstone et al. 2009; Kuiper et al. 2010; Abdo et al. 2009, 2013; Li et al. 2018). Here we perform pulsar timing analyses to select off-pulse intervals for our PWN study. The *Chandra* HRC data (Slane et al. 2002) are particularly useful for estimating the pulsar’s constant emission which may contaminate the PWN spectrum (Sections 2.4 and 2.5). So we reanalyze them here.

For a *Chandra* HRC data analysis, we extract events within an $R = 1''$ circular region with PI channels between 30 and 240. We then search for pulsation around the reported period of 65 ms using the H test (de Jager et al. 1989), and find pulsations in both HRC data sets (Fig. 1). We also perform a pulsation search in the *NuSTAR* data using an $R = 30''$ circle in the 3–79 keV band and find pulsations (Fig. 1). Because of very hard pulsed emission of the pulsar and *NuSTAR*’s excellent sensitivity at high energies (Madsen et al. 2015b), the source pulsations are detected easily in a short < 10 -ks interval. So we are able to perform a phase semi-coherent timing analysis using a double Gaussian function for the pulse profile. The data are sensitive enough to measure the first frequency derivative; the measured frequency and its derivative are $15.20102356(11) \text{ s}^{-1}$ and $-4.44(62) \times 10^{-11} \text{ s}^{-2}$ at the epoch MJD 58252.479. Results of pulsar timing and spectral analyses will be presented elsewhere. We show the measured pulse profiles in Figure 1 and select off-pulse intervals ($\phi=0.08\text{--}0.495$ and $0.575\text{--}1.0$) for the PWN studies below. Note that changing the off-pulse intervals slightly (e.g., $\phi=0.1\text{--}0.49$ and $0.59\text{--}1.0$) does not alter the results below.

2.3. X-ray image analysis

Because *NuSTAR* angular resolution is not sufficient to separate the pulsar from the PWN spatially, the pulsar’s constant emission may contaminate the PWN spectrum. This contamination can be estimated with high-resolution *Chandra* HRC data (e.g., PSR B1509–58; Chen et al. 2016), and so we use *Chandra* HRC observations to estimate the pulsar contamination in 3C 58.

We combine the HRC observations (Table 1) after aligning the images using the pulsar position and select on- and off-pulse intervals. The on-pulse intervals are shown in Figure 1. We use a rectangular region ($30'' \times 30''$) to include the torus-jet structure and have enough statistics, project the events onto the decl. direction, and produce brightness profiles of the on- and the off-pulse intervals in the 0.3–5 keV energy band (PI channels 22–343; Fig. 2). The profiles seem to have three components: a sharp peak $|D| < 1''$, a relatively broad shoulder $1'' \leq |D| \lesssim 4''$, and a flat component. The on-pulse profile (black) has a large core at $|D| < 1''$

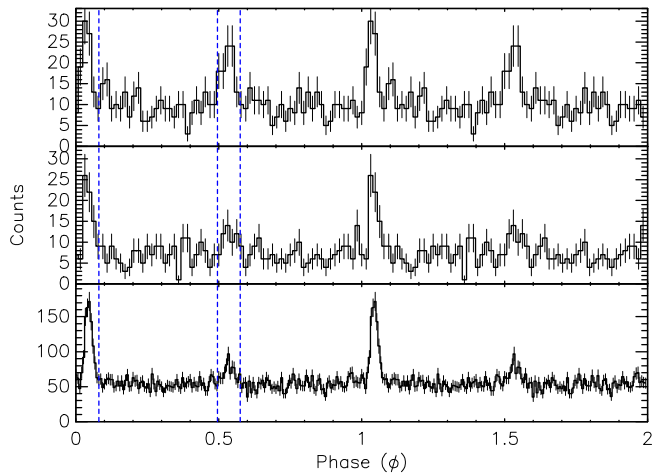


Figure 1. X-ray pulse profiles measured with *Chandra* (top and middle) and *NuSTAR* (bottom). Vertical blue lines show on-pulse intervals. Pulsations are detected with high significances: $H=57$, 33, and 599 from top to bottom. For the *Chandra* profiles, we use an $R = 1''$ region with the PIs 30–240 in Obs. IDs 1848 (top) and 2756 (middle). An $R = 30''$ circle and the 3–79 keV band are used for the *NuSTAR* profile.

but matches well with the off-pulse one (blue) at larger distances. So we assume that the central peak is the pulsar emission and the structures at $|D| > 1''$ are the PWN. The latter is estimated with a Gaussian function; we fit the off-pulse profile with a Gaussian plus constant function, ignoring the central $2''$ (pulsar component). The best-fit function is shown in the figure (red dashed). It is clear that the pulsar’s off-pulse emission (blue above red in Fig. 2) is very small compared to the PWN ($\sim 5\%$). We also verify that this fraction drops at higher energies. So using the off-pulse intervals for *NuSTAR* PWN studies will be appropriate because contamination of the pulsar’s constant (off-pulse) emission would be very small ($< 1\%$) in the > 3 keV band and large apertures $R \geq 1'$ used for *NuSTAR* data analyses (Sections 2.4 and 2.5).

Because of the synchrotron burn-off effect, the size of a young PWN is known to decrease with energy. This has been seen in some young PWNe (Nynka et al. 2014; An et al. 2014a; Madsen et al. 2015a), and here we produce images of the 3C 58 PWN in six energy bands using the *NuSTAR* data. In order to maximize the signal to noise ratio, we combine FPMA/B data together after aligning them using the central pulsar position. We extract events in the off-pulse intervals, and make images in six energy bands. We show the *NuSTAR* images together with *Chandra* ACIS contours in Figure 3. At low energies, elliptical morphologies similar to that of *Chandra* are seen. The PWN shrinks with increasing energy ; the observed half power diameters (HPDs)

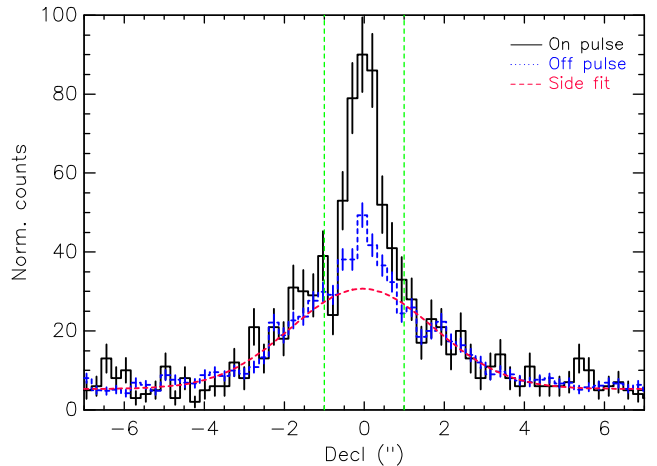


Figure 2. Time-normalized brightness profiles in the 0.3–5 keV band measured with the HRC data. The black and the blue lines show profiles for the on-pulse and the off-pulse intervals, respectively. The red dashed line denotes a fit to the $|D| > 1''$ off-pulse profile, representing the PWN emission. Vertical dashed lines (green) mark a central $2''$ region in which $> 95\%$ pulsar emission is contained.

decreases from $120 \pm 2''$ at 3 keV to $91 \pm 1''$ at 14 keV. These correspond to $101 \pm 2''$ and $68 \pm 2''$ when removing the instrumental PSF (An et al. 2014b) in quadrature. The source is detected up to 60 keV and the detection significance is $\sim 5\sigma$ in the 40–60 keV band for $R = 30''$ extraction.

2.4. Spatially-resolved Spectral Analysis

The spectrum and its radial variation of 3C 58 in the soft X-ray band (< 10 keV) were previously studied with *Chandra* ACIS data by Slane et al. (2004), where the authors found steepening of the spectrum with distance from the central pulsar. In that study, the spectrum was measured only out to $100''$ due to the limited field of view (FoV) and the contamination of a thermal shell (e.g., Bocchino et al. 2001). We extend this to a larger region and higher energies up to ~ 20 keV. Here we perform spectral analyses with the *NuSTAR* data and re-analyze the *Chandra* data for comparison with the *NuSTAR* results.

We extract *NuSTAR* events in the off-pulse intervals using an $R = 30''$ circular region and annular regions with width of $30''$ out to $3'$ to investigate radial variation of the PWN spectrum. Background events are extracted in the source-free regions of the detector chips in which the PWN is detected (mainly detector IDs 0 and 3). Spectral response files are generated for each region with the `nuproduct` tool with `extended=yes`. We group the spectra to have at least 100 events per energy bin and fit jointly all the spectra in the 3–20 keV band with absorbed power-law models having a com-

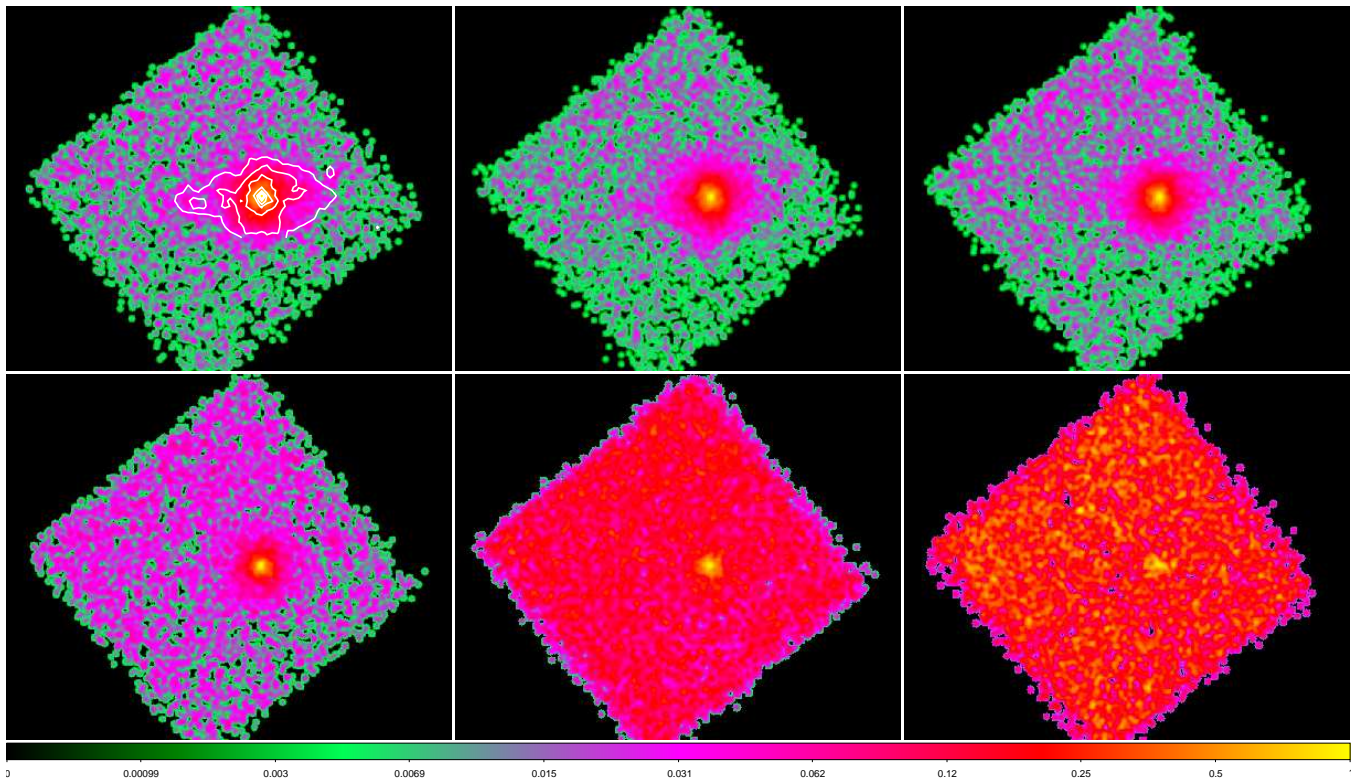


Figure 3. *NuSTAR* images of 3C 58 in six energy bands. The energy bands for the images are 3–4.5 keV, 4.5–7 keV, 7–12 keV, 12–20 keV, 20–40 keV, and 40–60 keV from left to right and top to bottom. The images are smoothed and the scales are adjusted to have a value of 1 at the maximum for better legibility. *Chandra* white contours are overlaid in the top-left panel for reference.

mon absorbing column density (N_{H}) which is held fixed at $4.5 \times 10^{21} \text{ cm}^{-2}$. The results are shown in Figure 4. Note that using a broader energy band (e.g., 3–60 keV) or different background regions does not change the results because the source dominates in the low-energy band below 20 keV.

For the *Chandra* spectral analysis, we use the ACIS data (Table 1). The central pulsar emission is removed using an exclusion region of an $R = 1''$ circle. This leaves $\sim 5\%$ pulsar contamination in the innermost region, but considering the very small duty of the pulsation (Fig. 1) it will be insignificant. We also check pile-up effects which are only a few % level just inside the central $1''$ (pulsar region) and smaller away from the pulsar. Source events are extracted from concentric annular regions with varying widths (between $2''$ and $15''$) out to $100''$ limited by the detector FoV for these subarray observations. Backgrounds are extracted from source-free regions. We generate response files for extended emission, group the spectra to have at least 20 events per bin, and jointly fit the spectra with absorbed power-law models in the 0.6–10 keV band; changing the energy range slightly does not alter the results. The results are shown in Figure 4. The spectral-index and the flux trends agree very well with the *NuSTAR*-measured

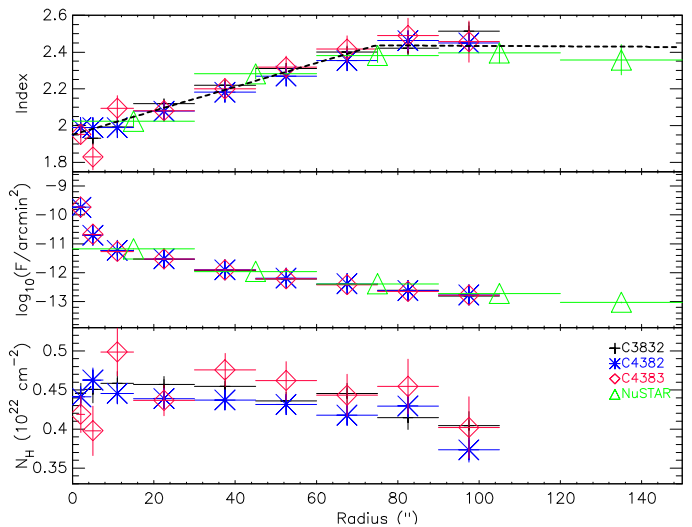


Figure 4. Radial variation of the PWN spectral parameters measured with *NuSTAR* and *Chandra*. Results of *Chandra* analyses are denoted in black (ObsID. 3832), blue (ObsID. 4382) and red (ObsID. 4383), and those of *NuSTAR* analyses are shown in green. *Top*: photon index variation. The best-fit broken-line function is shown in a dashed line. *Middle*: variation of the 3–10 keV brightness. *Bottom*: N_{H} variation measured with *Chandra*.

ones. The spectral index profile (top panel of Fig. 4) shows a break at $\sim 60\text{--}80''$ similar to that seen in a pre-

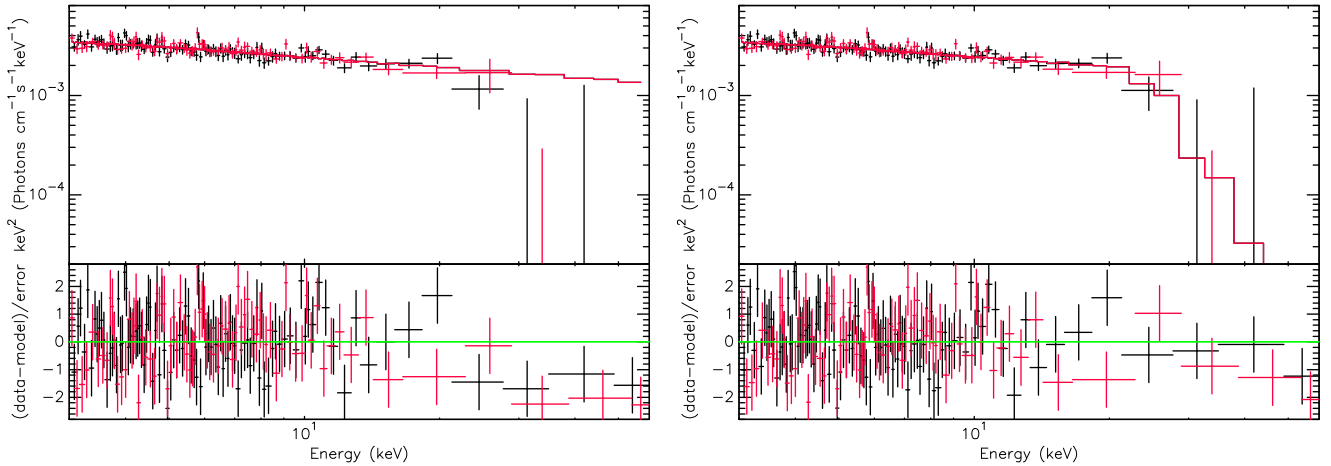


Figure 5. Spatially integrated *NuSTAR* spectra ($3'$) and residuals (bottom) after fitting. *Left*: power-law fit result. *Right*: broken power-law fit result.

Table 2. *NuSTAR* fit results for the spatially integrated spectra in the $R = 3'$ source region

model ^a	energy range (keV)	Γ	E_b ^b (keV)	Γ_2/α ^c	F_X ^d	χ^2/dof
PL	3–60	2.35 ± 0.02	11.5 ± 0.2	303.7/295
BPL	3–60	2.33 ± 0.02	23.2 ± 1.9	9.5 ± 8.4	9.0 ± 0.3	287.0/293
PLEXP	3–60	2.32 ± 0.03	30.9 ± 5.4	5 ± 6	9.1 ± 0.4	289.7/293

Notes. N_H is held fixed at $4.5 \times 10^{21} \text{ cm}^{-2}$

^aPL: power law. BPL: broken power law. PLEXP: power law with a super-exponential cutoff

^bBreak energy for BPL and cut-off energy for PLEXP

^cHard power-law index Γ_2 for BPL and the exponent index α for PLEXP

^d3–79 keV flux in units of $10^{-12} \text{ erg cm}^{-2} \text{ s}^{-1}$

vious study (Slane et al. 2004); our broken-line function fit suggests that the break point is $R_b = 75 \pm 4''$. We find that the measured N_H is slightly lower in the outer regions (Fig. 4 bottom), which is probably due to the contamination of a thermal shell as noted by Bocchino et al. (2001).

2.5. Spatially-integrated Spectral Analysis

Next we analyze spatially integrated spectra of the PWN to search for a spectral break as seen in other young PWNe (e.g., G21.5–0.9 and the Crab nebula; Nynka et al. 2014; Madsen et al. 2015a). Because combining *Chandra* and *NuSTAR* data is not ideal for this study due to cross-calibration effects (Madsen et al. 2015b), we focus on the *NuSTAR* data. We extract source events within an $R = 3'$ circle in the off-pulse intervals. Detector background is not uniform across the chips (Fig. 3), so we extract background events using circular regions of which area is proportional to the occupancy of the source region in each detector chip. We generate response files using the `nuproduct` tool with the `extended=yes` flag, group the spectra to have at least 100 events in each spectral bin, and fit the spectra in the 3–60 keV band with a power-law model. The

model explains the data with a null-hypothesis probability $p \sim 0.35$ but leaves a residual trend at high energies (Fig. 5 left). Motivated by the residual trend (deficit at high energies $>20 \text{ keV}$), we fit the spectra with a broken power-law (BPL) and a power-law with super-exponential-cutoff models (PLEXP), and find that these models improve the fit significantly with f -test probabilities of 2.5×10^{-4} and 10^{-3} , respectively. The results are shown in Figure 5 and Table 2. We also use different source extraction sizes ($R = 1'$ and $2'$) and find that the significance (PL vs. BPL) for the break drops as the size of the source extraction region decreases with $p \approx 0.2$ and $p \approx 0.04$ for $R = 1'$ and $R = 2'$ extraction regions, respectively.

Because background dominates above $\sim 25 \text{ keV}$, the results may change sensitively depending on the background selection. We therefore try to use different background regions for the $R = 3'$ source extraction: (1) extracting background as above (in four chips) but with the size and location of the background regions changing, and (2) extracting background events in one chip (detector ID 0) where the largest part of the PWN is detected (Fig. 3). Note that the latter is not ideal for background extraction given the inhomogeneity in back-

ground across the detector chips; we do this only for a test. The significance for the break (PL vs. BPL) changes depending on the background extraction between $p = 4 \times 10^{-5}$ for case (1) and $p = 3 \times 10^{-2}$ for case (2).

Next, we measure the PWN spectra in a $8' \times 5'$ diamond-shape region similar to the radio shape (e.g., Slane et al. 2008). Because large part of this region lies outside the FoV in the *Chandra* observations, we do not analyze the *Chandra* data. We obtain *NuSTAR* spectra and response files using the same method as described above, fit the spectra with a power-law model, and find that the spectral index is Γ is 2.34 ± 0.02 and the 3–79-keV flux is $11.8 \pm 0.2 \times 10^{-12}$ erg cm $^{-2}$ s $^{-1}$ similar to those of the $R = 3'$ spectrum. The high-energy residuals are also visible in these spectra, and a BPL model is preferred over a simple power law with $p=0.05\text{--}0.0003$ depending on the background selection.

We also analyze the spatially integrated *Chandra* spectrum using $R = 2'$ extraction for reference. In order to minimize contamination from the thermal shell, we ignore the low-energy data and fit the 3–7 keV spectra with a power-law model. We hold N_{H} fixed at the typical value of 4.5×10^{21} cm $^{-2}$, and measure $\Gamma = 2.25 \pm 0.03$ and $F_{3\text{--}10 \text{ keV}} = 6.14(6) \times 10^{-12}$ erg cm $^{-2}$ s $^{-1}$. Note that the results are not sensitive to the N_{H} value or the energy range. Although direct comparison with the *NuSTAR* results may not be adequate because of different PSF, we note that the power-law index is similar to a *NuSTAR*-measured one in $R = 2'$.

3. SED IN THE RADIO-TO-X-RAY BAND

With our X-ray and previous measurements (Slane et al. 2008; Planck Collaboration et al. 2016), we construct a low-energy SED of 3C 58 in the radio to X-ray band. Figure 6 shows the SED together with high-energy measurements (Li et al. 2018; Aleksić et al. 2014). For the X-ray data, we use the *NuSTAR* spectrum extracted from the diamond region (Section 2.5) similar to that used for extracting the radio-to-IR SED. Note that the hard X-ray SED aligns reasonably well with the previous *Chandra* one (Slane et al. 2004) which we do not use here because the measurement does not cover outer regions of the PWN. The improved X-ray measurement helps to determine accurately the break frequency between the IR and the X-ray bands which can provide an estimate of magnetic field or age for the synchrotron-loss dominating PWN (e.g., Torres et al. 2013). We therefore measure the break frequency by fitting the SED with phenomenological models.

We fit the IR ($1.4 \times 10^{11} < \nu < 10^{14}$ Hz) and the X-ray data ($10^{17} < \nu < 4 \times 10^{18}$ Hz) separately with

power-law functions. The frequency ranges are chosen to avoid the radio ($\nu \sim 10^{11}$ Hz) and the X-ray breaks ($\sim 5 \times 10^{18}$ Hz) which are assumed to be intrinsic to the electron distribution (e.g., Bucciantini et al. 2011). We extend the best-fit functions to find the frequency at which the two power-law functions cross (blue and red lines in Fig. 6 left). We also fit the SED ($1.4 \times 10^{11} < \nu < 6 \times 10^{18}$ Hz) with a broken power-law function (green) and find that the break frequency is between 4.3×10^{14} Hz and 3.6×10^{15} Hz and the degree of break is $\Delta\Gamma = 0.38 \pm 0.05$ with 1- σ confidence. Note that varying the frequency range for the fit or the *NuSTAR* flux (e.g., calibration uncertainty; Madsen et al. 2015b) does not alter the results significantly.

For a synchrotron-loss dominated PWN with homogeneous magnetic field, there is a simple relation among the frequency of the cooling break (ν_b), age of the PWN (t_{age}), and the magnetic field strength (B): $t_{\text{age}} = 4.12 \times 10^4 (\frac{B}{1\text{G}})^{-1.5} (\frac{\nu_b}{1\text{Hz}})^{-0.5}$ years (e.g., Slane et al. 2008). This relation can give us an estimate of one quantity if the other two are known. Figure 6 shows the relations between the age and the break frequency for various magnetic-field strengths. Our measurement of the break frequency and previous estimation of the age can be used to constrain the magnetic-field strength in 3C 58. The red box in the figure shows the previously-suggested parameter space for t_{age} and ν_b for 3C 58, and from this we infer B to be between $30\mu\text{G}$ and $200\mu\text{G}$.

4. DISCUSSION AND CONCLUSIONS

We analyzed new *NuSTAR* and archival *Chandra* data to measure the X-ray spectrum of 3C 58 and search for a spectral break in the X-ray band. We carefully selected off-pulse intervals so that the pulsar emission is ignorable in the *NuSTAR* data analyses. The size of the PWN decreases with increasing energy, which we attribute to the synchrotron burn-off effect. The radial profile of the spectral index breaks at $R \approx 80''$, and the spatially integrated X-ray spectrum of 3C 58 shows a hint of a spectral break at ≈ 25 keV.

A radial change (out to $\sim 100''$) of the 2.2–8 keV spectral index was measured for 3C 58 (Slane et al. 2004) previously. From this measurement, Tang & Chevalier (2012) inferred a maximum electron energy of 40 TeV using a diffusion model for an assumed equipartition magnetic-field strength of 80 G (Green & Scheuer 1992). Our studies made with *NuSTAR* revealed a similar radial trend of the X-ray spectrum to that measured with *Chandra* (Slane et al. 2004), and extended the measurements to higher energies ~ 20 keV and to a larger distance (Fig. 4). This then will increase the inferred max-

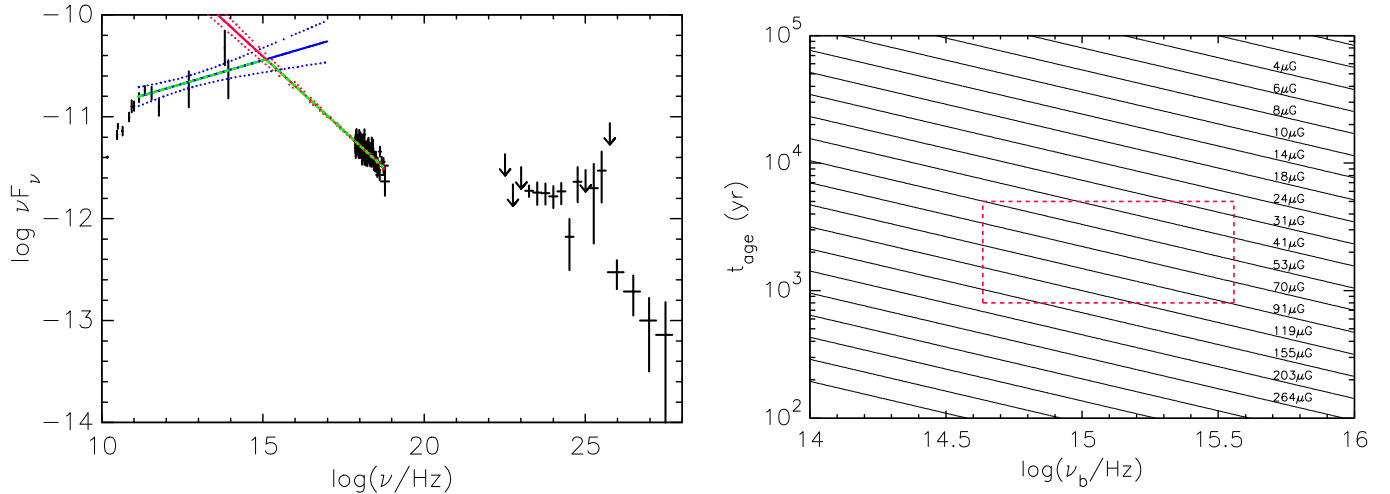


Figure 6. *Left:* a broadband SED of 3C 58. The radio-to-IR SED is taken from Slane et al. (2008) and Planck Collaboration et al. (2016), the X-ray SED is measured in this work, and the gamma-ray data are taken from Aleksić et al. (2014) and Li et al. (2018). Power-law fits with $1-\sigma$ confidence ranges to the lower-energy ($2 \times 10^{11} - 10^{14}$ Hz) and higher-energy ($10^{17} - 4 \times 10^{18}$ Hz) data are shown in blue and red, respectively. A broken power-law fit to the broadband data ($2 \times 10^{11} - 4 \times 10^{18}$ Hz) is shown in green. *Right:* relation between the PWN age and the break frequency for various magnetic-field strengths. The red box shows current estimations on the age and the break frequency.

imum electron energy because electrons should be able to emit higher-energy photons for the same magnetic field. Using analytic formulae (equations 8 and 14 of Tang & Chevalier 2012) and our measurements, we calculate the maximum electron energy to be ~ 200 TeV; this approximate calculation provides a rough estimate, but actual simulations need to be performed to improve the estimate. Note that we used $R_{\text{PWN}} = 2'$ (Bocchino et al. 2001) in our calculation even though the properties are measured out to $R \sim 3'$. This is because photons in the outermost region in the *NuSTAR* data are probably produced by PSF scattering.

The low-energy SED in the radio to X-ray band (Fig. 6 left) suggests a spectral (cooling) break $\Delta\Gamma \sim 0.4$ at $\sim 10^{15}$ Hz. From the measured frequency range for the cooling break and the assumed ages of 3C 58, we inferred the magnetic-field strength (assuming constant field over the PWN) to be $\sim 30\text{--}200 \mu\text{G}$. This observationally-estimated B agrees with the previous estimations based on SED modelings (Tanaka & Takahara 2013; Torres et al. 2013) or $\sim 40 \mu\text{G}$ estimated with MHD simulations (Porth et al. 2016). Note that Tanaka & Takahara (2013) and Torres et al. (2013) used the cooling break in their SED models, so the agreement was anticipated. While it is difficult to estimate both B and t_{age} simultaneously because of parameter degeneracy, a measurement of one parameter (e.g., magnetic field strength using radio polarization) will be very helpful to infer the other and to confirm whether or not the PWN is associated with SN 1181. Of course, the IR and the X-ray SED measurements also need to be improved

in order to determine the frequency of the cooling break more precisely.

We find a hint of a break in the spatially-integrated X-ray spectrum of 3C 58 at ~ 25 keV. The detection significance is relatively high for a larger extraction region, but the significance drops as the extraction region becomes smaller. This is perhaps because of decreasing statistics for smaller extraction regions. Although the detection significance is not very high and the degree of the break ($\Delta\Gamma$) is not well measured, we speculate on a possible reason. In synchrotron emission models for PWNe (e.g., Kennel & Coroniti 1984; Tang & Chevalier 2012), the synchrotron cooling pushes the high-energy cutoff in the electron distribution to low energies with time (i.e., distance from the pulsar), and so the integrated photon spectrum of a PWN is expected to be a simple power law in the X-ray band up to a frequency at which the maximum-energy electrons radiate. In these models, the 25-keV spectral break in the photon spectrum corresponds to the cutoff energy of the electron distribution, implying a maximum electron energy of ~ 140 TeV for an assumed magnetic-field strength of $80 \mu\text{G}$. Note that this is larger than 40 TeV inferred from a previous diffusion modeling (Tang & Chevalier 2012). Although detailed simulations with diffusion and particle transport are needed for a better estimation of the maximum electron energy, our estimation is of the same order of magnitude of previous works. Nevertheless, if the 25-keV break is real, it may imply that the injected electron distribution cuts off at a lower energy than assumed in SED models for 3C 58 (Tanaka & Takahara

2013; Torres et al. 2013; Li et al. 2018). So the models may need some modifications. The effect of the break is to change synchrotron and IC SEDs at the highest energies, but the changes are expected to be very small because of decreasing flux with energy (synchrotron) and the Klein-Nishina suppression (IC).

In a recent model (Lyutikov et al. 2018) existence of two populations of particles, accelerated by shock and magnetic reconnection in PWNe, are suggested. A spectrum of the latter population may extend to higher energies and make a small step in the spectrum when combined with the former. A hint of a spectral step is suggested in the Crab nebula at ~ 130 keV (Meyer et al. 2010; Lyutikov et al. 2018). So it will be interesting to see whether the spectrum of 3C 58 keeps curving down ≥ 25 keV (i.e., cutoff), or the break is actually a small step and another power-law spectrum appears at higher energies; the latter may imply another population of particles, i.e., acceleration mechanism in PWNe (Lyutikov et al. 2018). This can be tested in the hard X-ray and/or the soft gamma-ray bands with deeper *NuSTAR* and future *AMEGO* (McEney 2017) observations.

Our measurements of X-ray properties of 3C 58 add more information to the acceleration/emission models of PWNe. While current PWN models are able to reproduce the observed SED or the radial profile of the soft-X-ray spectral index, it is not clear whether the models can accommodate the hard X-ray properties, in particular, the possible spectral break. So confirming or disproving the existence of the break observationally is crucial. With the well measured broadband SED and the possible X-ray break, 3C 58 may give us new insights into particle acceleration and flow in PWNe.

We thank the anonymous referee for the careful reading of the paper and insightful comments. This research was supported by Basic Science Research Program through the National Research Foundation of Korea (NRF) funded by the Ministry of Science, ICT & Future Planning (NRF-2017R1C1B2004566).

Facilities: CXO, NuSTAR

Software: HEASoft (v6.24; HEASARC 2014), CIAO (v4.10; Fruscione et al. 2006), XSPEC (Arnaud 1996)

REFERENCES

- Abdo, A. A., Ackermann, M., Ajello, M., et al. 2009, *ApJL*, 699, L102
- Abdo, A. A., Ajello, M., Allafort, A., et al. 2013, *ApJS*, 208, 17
- Aleksić, J., Ansoldi, S., Antonelli, L. A., et al. 2014, *A&A*, 567, L8
- An, H., Madsen, K. K., Reynolds, S. P., et al. 2014a, *ApJ*, 793, 90
- An, H., Madsen, K. K., Westergaard, N. J., et al. 2014b, in *Proc. SPIE*, Vol. 9144, *Space Telescopes and Instrumentation 2014: Ultraviolet to Gamma Ray*, 91441Q
- Arnaud, K. A. 1996, in *Astronomical Society of the Pacific Conference Series*, Vol. 101, *Astronomical Data Analysis Software and Systems V*, ed. G. H. Jacoby & J. Barnes, 17
- Bietenholz, M. F., Kassim, N. E., & Weiler, K. W. 2001, *ApJ*, 560, 772
- Bocchino, F., Warwick, R. S., Marty, P., et al. 2001, *A&A*, 369, 1078
- Bucciantini, N., Arons, J., & Amato, E. 2011, *MNRAS*, 410, 381
- Chen, G., An, H., Kaspi, V. M., et al. 2016, *ApJ*, 817, 93
- de Jager, O. C., Raubenheimer, B. C., & Swanepoel, J. W. H. 1989, *A&A*, 221, 180
- Fesen, R. A. 1983, *ApJL*, 270, L53
- Fruscione, A., McDowell, J. C., Allen, G. E., et al. 2006, in *Proc. SPIE*, Vol. 6270, *Society of Photo-Optical Instrumentation Engineers (SPIE) Conference Series*, 62701V
- Green, D. A., & Scheuer, P. A. G. 1992, *MNRAS*, 258, 833
- Harrison, F. A., Craig, W. W., Christensen, F. E., et al. 2013, *ApJ*, 770, 103
- Kargaltsev, O., Klingler, N., Chastain, S., & Pavlov, G. G. 2017, in *Journal of Physics Conference Series*, Vol. 932, *Journal of Physics Conference Series*, 012050
- Kennel, C. F., & Coroniti, F. V. 1984, *ApJ*, 283, 694
- Kothes, R. 2013, *A&A*, 560, A18
- Kuiper, L., Hermsen, W., Urama, J. O., et al. 2010, *A&A*, 515, A34
- Li, J., Torres, D. F., Lin, T. T., et al. 2018, *ApJ*, 858, 84
- Livingstone, M. A., Ransom, S. M., Camilo, F., et al. 2009, *ApJ*, 706, 1163
- Lyutikov, M., Temim, T., Komissarov, S., et al. 2018, *ArXiv e-prints*, arXiv:1811.01767

- Madsen, K. K., Reynolds, S., Harrison, F., et al. 2015a, *ApJ*, 801, 66
- Madsen, K. K., Harrison, F. A., Markwardt, C. B., et al. 2015b, *ApJS*, 220, 8
- McEney, J. E. 2017, in *AAS/High Energy Astrophysics Division*, Vol. 16, *AAS/High Energy Astrophysics Division #16*, 103.13
- Meyer, M., Horns, D., & Zechlin, H.-S. 2010, *A&A*, 523, A2
- Murray, S. S., Slane, P. O., Seward, F. D., Ransom, S. M., & Gaensler, B. M. 2002, *ApJ*, 568, 226
- Nynka, M., Hailey, C. J., Reynolds, S. P., et al. 2014, *ApJ*, 789, 72
- Planck Collaboration, Arnaud, M., Ashdown, M., et al. 2016, *A&A*, 586, A134
- Porth, O., Vorster, M. J., Lyutikov, M., & Engelbrecht, N. E. 2016, *MNRAS*, 460, 4135
- Reynolds, S. P. 2009, *ApJ*, 703, 662
- Reynolds, S. P., Pavlov, G. G., Kargaltsev, O., et al. 2017, *SSRv*, 207, 175
- Roberts, D. A., Goss, W. M., Kalberla, P. M. W., Herbstmeier, U., & Schwarz, U. J. 1993, *A&A*, 274, 427
- Sironi, L., Keshet, U., & Lemoine, M. 2015, *SSRv*, 191, 519
- Slane, P., Helfand, D. J., Reynolds, S. P., et al. 2008, *ApJL*, 676, L33
- Slane, P., Helfand, D. J., van der Swaluw, E., & Murray, S. S. 2004, *ApJ*, 616, 403
- Slane, P. O., Helfand, D. J., & Murray, S. S. 2002, *ApJL*, 571, L45
- Stephenson, F. R. 1971, *QJRAS*, 12, 10
- Tanaka, S. J., & Takahara, F. 2013, *MNRAS*, 429, 2945
- Tang, X., & Chevalier, R. A. 2012, *ApJ*, 752, 83
- Torii, K., Slane, P. O., Kinugasa, K., Hashimoto-dani, K., & Tsunemi, H. 2000, *PASJ*, 52, 875
- Torres, D. F., Cillis, A. N., & Martín Rodríguez, J. 2013, *ApJL*, 763, L4